Perturbation analysis of nonlinear evanescent waves in a one-dimensional monatomic chain

Lezheng Fang
School of Mechanical Engineering, Georgia Institute of Technology, Atlanta, Georgia 30332, USA

Michael J. Leamy*
School of Mechanical Engineering, Georgia Institute of Technology, Atlanta, Georgia 30332, USA

(Received 5 November 2021; accepted 23 December 2021; published 5 January 2022)

This paper investigates evanescent waves in one-dimensional nonlinear monatomic chains using a first-order Lindstedt-Poincaré approach. Perturbation approaches applied to traveling waves in similar chains have predicted weakly nonlinear phenomena such as dispersion shifts and amplitude-dependent stability. However, nonlinear evanescent waves have received sparse attention, even though they are expected to serve a critical role in nonlinear interface problems. To aid in their analysis, the nonlinear evanescent waves are categorized herein as either complete or transitional evanescent waves. Complete evanescent waves, including linear evanescent waves, attenuate to zero amplitude in the far field. Transitional evanescent waves, only occurring in softening systems, attenuate to a nontrivial amplitude in the far field, regardless of the initial amplitude, resulting in a saturation effect. For both cases, the presented perturbation approach reveals that the imaginary wave number in the evanescent field is a function of space, rather than a constant value as in its linear counterpart. It also reveals that hardening and softening nonlinearity slow and accelerate the near-field decay, respectively. The predictions obtained from the perturbation approach are verified using numerical simulations with both initial-condition and boundary-continuous excitation, documenting strong agreement.

DOI: 10.1103/PhysRevE.105.014203

I. INTRODUCTION

The study of wave propagation in linear periodic structures has a long history due to its relevance in a wide range of physical systems [1,2] and broad applications in science and engineering [3–7]. Recently, extensive research has focused on *nonlinear* periodic structures as nonlinearity can introduce amplitude dependency, $\mathcal{PT}$-symmetry breaking, bifurcation phenomena, extra-harmonic generation, subharmonic band gaps, and other behavior missing from linear systems [8–13]. A signature behavior of nonlinear periodic structures is amplitude-dependent dispersion and frequency corrections (or "shifts"), usually discussed in relation to nonlinear band structure. Nonlinear band structure for propagating waves in a variety of systems has been computed using the harmonic balance method [14–16], homotopy analysis [17,18], and a variety of perturbation approaches [19–25]. In weakly nonlinear systems, perturbation approaches are preferred since they yield closed-form, analytical expressions for the band structure. Using the Lindstedt-Poincaré and multiple scales methods to uncover amplitude-dependent band structure in discrete systems, researchers have uncovered the same frequency corrections using either method [20–22]; however, the multiple scales method enables solution of a broader class of problems, including propagation of multiple plane waves and their time-dependent interactions [21,26,27]. Very recently, Jiao and Gonella [28] showed that for boundary excited waves the dispersion shift occurs for both frequency and wave number.

Compared to numerous studies on nonlinear dispersion and band structure associated with traveling waves, sparse attention has been paid to nonlinear evanescent waves. Narisetti *et al.* [20] briefly considered nonlinear evanescent waves in a larger study on propagating waves and used the propagating solutions to inform an approximate frequency correction for evanescent waves. Khajehtourian and Hussein [29] employed a transfer matrix method and plotted the amplitude-dependent band structure for both traveling and evanescent waves. In addition, Chakraborty and Mallik [30] documented a wave-form transition phenomenon in a softening nonlinear system, where an evanescent wave evolves into a traveling wave. The majority of these research efforts emphasize the nonlinear effect as shifted dispersion curves in the imaginary wave-number domain and only provide qualitative predictions on the attenuation envelope. These features are, however, vital to certain problems such as wave propagation through linear-nonlinear and nonlinear-nonlinear material interfaces, where evanescent waves are needed to match the displacement and stress at interfaces [31].

Motivated by the need for a rigorous analytical treatment of nonlinear evanescent waves, for use in the aforementioned interface problems and others, we develop an evanescent-specific perturbation approach for predicting amplitude-dependent imaginary wave numbers and attenuation envelopes focusing firstly on weakly nonlinear monatomic chains. We employ the Lindstedt-Poincaré method to the first order, and we describe the imaginary wave number as a

*michael.leamy@me.gatech.edu

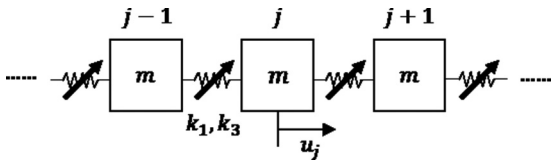

FIG. 1. The schematic of the studied nonlinear monatomic system.

function of space (vis-à-vis a constant). Hence, we show that in lieu of the conventional dispersion diagram, tracking the spatially dependent imaginary wave numbers and attenuation envelopes accurately predicts the spatial profile of nonlinear evanescent waves. Based on their frequency location relative to nonlinear and linear stopband, we categorize the nonlinear evanescent waves as one of two types: (i) complete evanescent waves and (ii) transitional evanescent waves. For transitional evanescent waves, we analyze the wave transition phenomenon and discover an amplitude-saturation effect. We then conduct numerical simulations to verify the analytical results. Lastly, we discuss the effect of different excitation methods (initial versus boundary excitation) on the resultant evanescent waves and document the saturation amplitude difference induced by the wave-number band-clipping effect.

II. SYSTEM DESCRIPTION

We consider a one-dimensional monatomic chain with adjacent masses coupled by an elastic spring with linear k_1 and cubic k_3 stiffness, as depicted in Fig. 1. The equation of motion is given as

$$m\ddot{u}_j + k_1(2u_j - u_{j-1} - u_{j+1}) + \epsilon k_3(u_j - u_{j-1})^3 + \epsilon k_3(u_j - u_{j+1})^3 = 0, \tag{1}$$

where j is the index of an arbitrary mass and u_j is its displacement. The parameter ϵ represents a small quantity denoting weak nonlinearity, which also serves as a bookkeeping device [32] in the subsequent perturbation approach. A positive coefficient ϵk_3 corresponds to a hardening nonlinear system, while a negative one corresponds to a softening one. Note that the quadratic nonlinearity is not considered in this study since its effect on dispersion shifts does not occur until higher orders in the analysis [24].

The monatomic system we study herein not only serves as a cornerstone to understand the nonlinear evanescent field, but arises in a multitude of physical systems at varying scales. In anharmonic three-dimensional crystals, the monatomic system represents acoustic wave propagation in the [100], [110], and [111] directions. In electromagnetics, the nonlinear monatomic system governs waves in macroscale media where cubic terms arise from the Kerr nonlinearity [22,33,34] and in acoustics where weak cubic stiffness can arise from material or geometric nonlinearity [35,36].

III. PERTURBATION ANALYSIS

We briefly review the nonlinear dispersion shift for traveling waves in the monatomic chain and then present the analysis for nonlinear complete evanescent waves and transitional evanescent waves.

Introducing the nondimensional time $\tau = \omega t$, the linear natural frequency $\omega_n = \sqrt{k_1/m}$, and the normalized cubic stiffness $\Gamma = k_3/k_1$, Eq. (1) can be rewritten as

$$\bar{\omega}^2 \frac{d^2u_j}{d\tau^2} + (2u_j - u_{j-1} - u_{j+1}) + \epsilon\Gamma(u_j - u_{j-1})^3 + \epsilon\Gamma(u_j - u_{j+1})^3 = 0, \tag{2}$$

where $\bar{\omega} = \omega/\omega_n$ denotes the nondimensional frequency.

According to the Lindstedt-Poincaré approach [32], we introduce asymptotic expansions for the displacement and frequency,

$$u_j = u_j^{(0)} + \epsilon u_j^{(1)} + O(\epsilon^2), \tag{3}$$

$$\bar{\omega} = \omega_0 + \epsilon\omega_1 + O(\epsilon^2). \tag{4}$$

Updating Eq. (2) yields an expanded equation of motion,

$$\omega_0^2 \frac{d^2u_j^{(0)}}{d\tau^2} + \epsilon\left(\omega_0^2 \frac{d^2u_j^{(1)}}{d\tau^2} + 2\omega_0\omega_1 \frac{d^2u_j^{(0)}}{d\tau^2}\right) = -\left(2u_j^{(0)} - u_{j-1}^{(0)} - u_{j+1}^{(0)}\right) - \epsilon\left(2u_j^{(1)} - u_{j-1}^{(1)} - u_{j+1}^{(1)}\right) - \epsilon\Gamma\left[\left(u_j^{(0)} - u_{j-1}^{(0)}\right)^3 + \left(u_j^{(0)} - u_{j+1}^{(0)}\right)^3\right] + O(\epsilon^2) = 0. \tag{5}$$

We next separate the expanded equation into orders of ϵ up to the second order,

$$\epsilon^0: \quad \omega_0^2 \frac{d^2u_j^{(0)}}{d\tau^2} + \left(2u_j^{(0)} - u_{j-1}^{(0)} - u_{j+1}^{(0)}\right) = 0, \tag{6}$$

$$\epsilon^1: \omega_0^2 \frac{d^2u_j^{(1)}}{d\tau^2} + \left(2u_j^{(1)} - u_{j-1}^{(1)} - u_{j+1}^{(1)}\right) = -2\omega_0\omega_1 \frac{d^2u_j^{(0)}}{d\tau^2} - \Gamma\left[\left(u_j^{(0)} - u_{j-1}^{(0)}\right)^3 + \left(u_j^{(0)} - u_{j+1}^{(0)}\right)^3\right]. \tag{7}$$

A. Traveling waves

For traveling waves, with real wave number μ, the zeroth-order equation, Eq. (6), admits a plane-wave solution

$$u_j^{(0)} = \frac{A}{2} e^{i\mu j} e^{-i\tau} + \text{c.c.}, \tag{8}$$

where herein c.c denotes the complex conjugate of all preceding terms, and A denotes the complex wave amplitude. Substituting Eq. (8) into Eq. (6) yields the zeroth-order (linear) dispersion relation

$$\omega_0 = \sqrt{2 - 2\cos(\mu)}. \tag{9}$$

Next, updating the first-order equation, Eq. (7), with the zeroth-order solution, and eliminating secular terms on the right-hand side, yields an expression for the corrected frequency ω_1 and, ultimately, the nonlinear dispersion

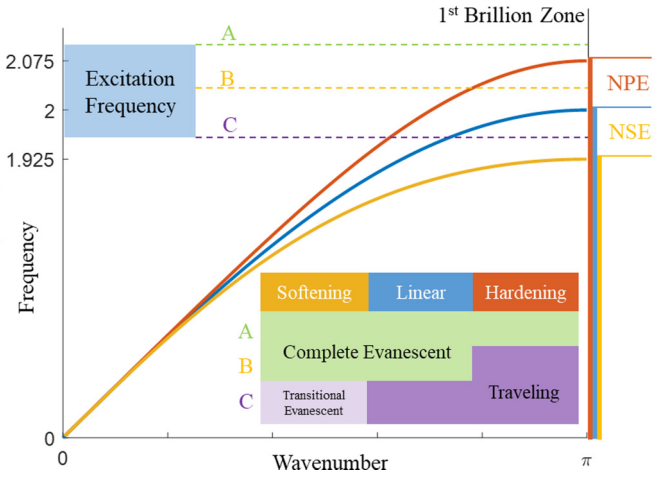

FIG. 2. Nonlinearly shifted dispersion for propagating waves (i.e., real wave numbers) in a monatomic chain, with amplitude $|A| = 0.5$. Blue, red, and yellow curves represent the linear, hardening, and softening nonlinear dispersions, respectively. The corresponding cutoff frequencies are marked on the vertical axis. The nonlinear passband extension (NPE) and nonlinear stopband extension (NSE) are indicated to the right. Three example signal frequencies and their corresponding wave forms in each system are presented in the embedded table.

relationship,

$$\bar{\omega}(\mu;A) = \sqrt{2[1-\cos(\mu)]} + \epsilon\frac{3\Gamma|A|^2[\cos(2\mu)-4\cos(\mu)+3]}{4\sqrt{2[1-\cos(\mu)]}} + O(\epsilon^2), \tag{10}$$

where the second term on the right-hand side captures the amplitude-dependent nonlinear correction (or shift). Further derivation details can be found in Ref. [20]. We note that at small amplitudes the cutoff frequency of the nonlinear passband is given by

$$\bar{\omega}_{\text{cutoff}} \equiv \bar{\omega}(\mu \equiv \pi) = 2 + 3\epsilon\Gamma|A|^2. \tag{11}$$

As illustrated in Fig. 2, a hardening nonlinearity broadens the passband by shifting dispersion branches upwards, resulting in a nonlinear passband extension, while a softening one lessens the passband by shifting branches downwards, resulting in a nonlinear stopband extension (NSE). Note that the shifts in the schematic are amplified for graphical illustration. Above the (nonlinear) cutoff frequency, the wave number contains an imaginary component which generates an amplitude-decaying evanescent field. In a linear system, this imaginary component is only a function of frequency and remains constant as the wave propagates [37]. However, in a nonlinear system, the amplitude attenuation will generate a spatially dependent dispersion correction, which in turn will influence the local attenuation.

We categorize two types of evanescent waves, namely, complete evanescent waves and transitional evanescent waves. The former, to include linear evanescent waves, denotes an evanescent wave which asymptotically approaches zero amplitude in the far field, while the latter denotes a nonlinear wave-form transition resulting in a finite amplitude in the far field. As suggested in Fig. 2's embedded table, a complete evanescent wave occurs when a signal's frequency is above both linear and nonlinear cutoff frequencies, whereas a transitional evanescent wave only occurs in softening systems, when the frequency falls in the NSE, below the linear cutoff frequency. These two types of evanescent waves are discussed in detail in the following two subsections.

B. Complete evanescent waves

First we discuss complete evanescent waves resulting from excitations in the mutual band gap of linear and nonlinear systems.

Without loss of generality, we study an arbitrary section of the evanescent field composed of three consecutive masses. Assuming the amplitude attenuation in this section is relatively small such that the imaginary wave number does not vary locally, we again seek a plane-wave solution satisfying Eq. (6),

$$u^{(0)}_{j+\kappa} = \frac{A}{2}e^{i[\kappa\mu-\tau]} + \text{c.c.}, \quad \kappa = -1, 0, 1, \tag{12}$$

where $\mu = \mu_r + i\mu_i$ denotes the complex wave number at the considered section, and the complex amplitude A is associated with the jth mass. Note that Eq. (12) is identical to Eq. (8) for the three masses considered with the exception of a complex wave number. Substituting Eq. (12) into Eq. (6) yields the complete evanescent wave's zeroth-order dispersion relationship,

$$\omega_0 = \sqrt{2 - e^{i(\mu_r+i\mu_i)} - e^{-i(\mu_r+i\mu_i)}}. \tag{13}$$

To ensure the frequency is real, the real component μ_r must equal either 0 or π. For the monatomic chain's acoustic branch, μ_r equates to π at the right edge of the Brillouin zone and maintains this value throughout the band gap [37]. Thus, Eq. (13) can be rewritten as

$$\omega_0 = \sqrt{2 + 2\cosh(\mu_i)}. \tag{14}$$

Note that if a grounded monatomic chain, or a chain with multiple degrees of freedom per unit cell, is considered, the real wave-number component may take on the value of 0 in at least one of the band gaps.

Next, we update Eq. (7) with the zeroth-order solution and eliminate secular terms, yielding

$$\omega_0\omega_1 - \frac{3\Gamma A\bar{A}}{4}\left(\frac{3}{2}e^{-\mu_i} + \frac{3}{2}e^{-2\mu_i} + \frac{1}{2}e^{-3\mu_i} + 1 + \frac{3}{2}e^{\mu_i} + \frac{3}{2}e^{2\mu_i} + \frac{1}{2}e^{3\mu_i}\right) = 0. \tag{15}$$

The first-order frequency correction term then follows,

$$\omega_1 = \frac{3\Gamma|A|^2(e^{3\mu_i}+1)(e^{\mu_i}+1)^3}{8\omega_0 e^{3\mu_i}}. \tag{16}$$

The nonlinear frequency correction is an even function of imaginary wave number μ_i, indicating reciprocity due to geometric symmetry. Note that the obtained solution is fundamentally different from the results one might obtain

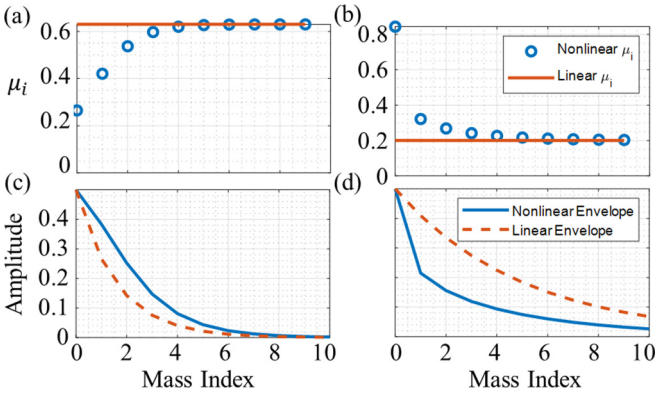

FIG. 3. Results for nonlinear and linear complete evanescent waves. The top row depicts the evolution of the imaginary wave number along the downstream direction, while the bottom row translates the imaginary wave number into a discrete attenuation envelope; the left column corresponds to a hardening nonlinear system, and the right column corresponds to a softening system.

by inserting $\mu = \mu_r + i\mu_i$ into the traveling-wave solution, Eq. (10), as done in Ref. [20] to obtain an approximate evanescent solution. Such an approach conflicts with an assumption made early in the perturbation analysis that the wave number is strictly real (since the focus was on traveling waves) and thus the complex conjugate of $e^{i\mu}$ is $e^{-i\mu}$, which is violated for complex μ.

Combining Eqs. (16) and (14) yields the full expression of the first-order perturbation result for the complete evanescent wave,

$$\bar{\omega} = \sqrt{2 + 2\cosh(\mu_i)} + \epsilon \frac{3\Gamma |A|^2 (e^{3\mu_i} + 1)(e^{\mu_i} + 1)^3}{8\sqrt{2 + 2\cosh(\mu_i)} e^{3\mu_i}}. \quad (17)$$

This equation specifies the frequency for a given amplitude and imaginary wave-number component at the jth mass.

Alternatively, for a given frequency and amplitude, Eq. (17) provides the imaginary wave-number component at the section of interest, such that Eq. (12) can then be employed to find the amplitudes of the neighboring masses (i.e., for $\kappa = -1$ and 1). We pursue this approach to compute the entire evanescent wave field, as follows. Once the neighboring mass amplitudes are determined, we shift the section location by one unit, such that, for example, the neighboring mass, $j + 1$, becomes the center of the new section. The amplitude of the $j + 2$ mass is computed using Eqs. (17) and (12) with A now representing the amplitude of the $j + 1$ mass. Repeating this procedure yields the entire attenuation envelope. Due to the validity of the perturbation approach requiring small amplitudes, we only follow this procedure in the evanescent (or downstream) direction since the opposite direction yields monotonically increasing amplitudes. We present results from this procedure next.

In Fig. 3 we compare evanescent quantities for nonlinear monatomic systems, corresponding to hardening and softening nonlinearity, with those for a linear monatomic chain. Figures 3(a) and 3(c) feature a hardening nonlinearity ($\epsilon\Gamma = 0.1$) with an excitation amplitude of 0.5 operating at a frequency of 2.1, above the nonlinear cutoff frequency specified by Eq. (11). This frequency choice is represented by "Excitation Frequency A" in Fig. 2. Figures 3(b) and 3(d) consider a softening nonlinearity ($\epsilon\Gamma = -0.1$) with the same excitation amplitude as the hardening case but at a frequency of 2.01 to ensure small initial attenuation. This frequency choice is represented by "Excitation Frequency B" in Fig. 2. In both cases, the linear system's imaginary wave-number components are positive constants indicated by red straight lines in Figs. 3(a) and 3(b), resulting in exponentially decaying dash-line envelopes in Figs. 3(c) and 3(d). In contrast, as the nonlinear systems' evanescent waves (blue lines) progress along the chain, as expected, their amplitudes decrease and their imaginary wave-number components gradually approach the linear system's constant value. Since the frequencies considered in both hardening and softening systems are above the linear cutoff frequency, the imaginary wave-number components approach nonzero, constant values, resulting in complete amplitude decay in the far field. Hence, we choose to term these "complete evanescent waves."

The presence of nonlinearities fundamentally alters the evanescent wave dynamics. As seen in Figs. 3(a) and 3(c), the nonlinear imaginary component of the wave number in a hardening system begins with a lower value, and thus a slower amplitude decay in the near field, compared to its linear counterpart. The softening nonlinear system, as seen in Figs. 3(b) and 3(d), results in an initial imaginary wave-number component higher than that of its linear counterpart, which induces a rapid drop in the near-field amplitude. We note further that the attenuation envelope of a nonlinear complete evanescent wave deviates from an exponential.

C. Transitional evanescent waves

In addition to complete evanescent waves, softening systems exhibit a second evanescent wave for frequencies lying in the NSE. This type of evanescent wave attenuates in the near field, but maintains a finite amplitude in the far field. We, therefore, choose to term it a "transitional evanescent wave."

A transitional evanescent wave occurs at frequencies in the NSE, as represented by "Excitation Frequency C" in Fig. 2. In the near field, such a wave attenuates due to its location in the nonlinear band gap. However, as the wave amplitude decreases, the corresponding nonlinear shift of the traveling-wave dispersion also decreases such that the dispersion curve rises from its initially shifted position. In this process, the NSE region shrinks until the lower boundary of the NSE aligns with the excitation frequency or, equivalently, the excitation frequency intersects the traveling-wave dispersion curve at the right edge of the Brillouin zone. At this diminished wave amplitude, which we term the "saturation amplitude," the imaginary wave-number component reaches zero, and therefore the wave maintains its amplitude from this location onward.

For a given monatomic chain, the saturation amplitude A_{sat} is a sole function of the excitation frequency and is independent of the excitation amplitude. It can be calculated by equating the nonlinear cutoff frequency to the excitation frequency, $\omega_{\text{cutoff}} = \bar{\omega}$, in Eq. (11),

$$A_{\text{sat}} = \sqrt{\frac{\bar{\omega} - 2}{3\epsilon\Gamma}}. \quad (18)$$

Note that the saturation amplitude is only valid in softening systems (i.e., $\epsilon\Gamma < 0$).

For the saturation envelope, the perturbation result in Eq. (17) yields accurate results for the transitional evanescent wave when the saturation amplitude is small [see Figs. 7(a) and 7(b) in the Appendix]. When the saturation amplitude is considerably larger, however, the imaginary wave-number component changes rapidly in the near field such that the local imaginary component of the wave number, μ_i, cannot be treated as a constant for three consecutive masses, as done earlier. Consequently, Eq. (17) generates overestimated imaginary wave numbers, such that the amplitude of the next neighboring mass may drop below the saturation value [see Figs. 7(c)–7(h) in the Appendix].

To address this issue, we modify the zeroth-order solution form such that the wave amplitude admits a local exponential decay in any three consecutive masses considered. We thus seek a solution ansatz of the form Eq. (19),

$$u_{j+\kappa}^{(0)} = \tfrac{1}{2}[(|A| - A_{\text{sat}})e^{-\kappa\zeta} + A_{\text{sat}}]e^{i[\theta+\kappa\mu_r-\tau]} + \text{c.c.},$$
$$\kappa = -1, 0, 1, \tag{19}$$

where ζ denotes the local decay factor at the section centered at the jth mass, and the complex amplitude A is expressed in the polar form $|A|e^{i\theta}$. This ansatz ensures the wave amplitude in the field is strictly greater than the saturation amplitude. We determine ζ after the nonlinear dispersion expression is derived. We note that the zeroth-order solution sought for complete evanescent waves [i.e., Eq. (12) in Sec. III B] can be treated as a special case of Eq. (19) by setting A_{sat} to zero and ζ to μ_i.

Substituting Eq. (19) into Eq. (6) with $\mu_r = \pi$ yields the zeroth-order dispersion relationship for transitional evanescent waves,

$$\omega_0 = \sqrt{\frac{2}{|A|}[|A| + A_{\text{sat}} + \cosh(\zeta)(|A| - A_{\text{sat}})]}. \tag{20}$$

We next update Eq. (7) with Eqs. (19) and (20). By eliminating the secular terms in this updated equation, we can derive the nonlinear correction ω_1 as a function of the amplitude $|A|$ and the decay factor ζ, such that the full expression of the first-order perturbation result for transitional evanescent waves is

$$\bar{\omega} = \sqrt{\frac{1}{|A|}(2|A| + \alpha + \beta)} + \epsilon\frac{3\Gamma}{8\sqrt{|A|(2|A| + \alpha + \beta)}}\,[2|A|^3 + 3|A|^2(\alpha + \beta) + 3|A|(\alpha^2 + \beta^2) + \alpha^3 + \beta^3], \tag{21}$$

where

$$\alpha = (|A| - A_{\text{sat}})e^{\zeta} + A_{\text{sat}}, \tag{22}$$

$$\beta = (|A| - A_{\text{sat}})e^{-\zeta} + A_{\text{sat}}. \tag{23}$$

Similar to Sec. III B, at a given signal frequency $\bar{\omega}$ and starting amplitude A, we find the local decay factor ζ via inversion of Eq. (21). Once the local decay factor ζ is obtained for the initial triplet of masses, we compute the amplitude of the downstream neighboring mass in Eq. (19) and shift the section location by one unit. The computed neighboring mass's amplitude is now at the center of the new section where we calculate its corresponding local decay factor ζ. Repeating this procedure yields the entire transitional evanescent wave envelope in the downstream direction.

We present the results for an example transitional evanescent wave in Figs. 4(a) and 4(b) where the initial amplitude equals 0.5 and the frequency $\bar{\omega}$ equals 1.95. For numerical reference, the saturation amplitude at this frequency is $A_{\text{sat}} = 0.408$ according to Eq. (18). To assist in interpreting the nonlinear behavior, we derive an equivalent imaginary wave-number component at each mass by comparing its amplitude to its downstream neighbor, $\mu_i^{\text{eq}}(j) \equiv \ln(\frac{A(j)}{A(j+1)})$, and also plot it in Fig. 4(a).

In Fig. 4(a), we observe the decay factor ζ and the equivalent imaginary component of the wave number μ_i^{eq} steadily decrease as the wave progresses. Compared to the slow decrease in ζ, μ_i^{eq} experiences a rapid decrease. It is this rapid change that necessitated the need to modify the zeroth-order solution approach. Further, we observe the local decay factor ζ converges to a constant value in the far field. This convergence indicates that when the wave amplitude approaches the saturation value, as plotted in Fig. 4(b), the local decay factor can be treated as a constant, and the attenuation is essentially an exponential decay to the saturation amplitude. This convergence value can be derived by introducing a small

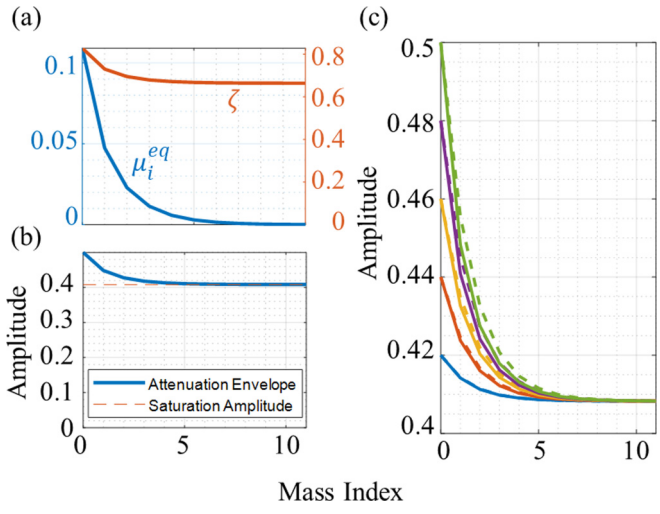

FIG. 4. Perturbation results for transitional evanescent waves. (a) The evolution of the local decay factor ζ and the equivalent imaginary wave-number component μ_i^{eq} in the downstream direction. (b) The nonlinear attenuation envelope and the saturation amplitude. (c) Attenuation envelopes initiated at varying amplitudes. The solid and dashed curves represent envelopes obtained from a spatially varying ζ and a uniform exponential index ζ^* computed from the convergence, respectively.

perturbation to the amplitude in Eq. (21) such that it lies just above the saturation amplitude, i.e., $|A| = A_{\text{sat}} + \delta$, where δ denotes a small positive perturbation. Taylor expanding the updated Eq. (20) around δ yields

$$\bar{\omega} = 2 + 3\epsilon\Gamma A_{\text{sat}}^2 + \left(\frac{2\cosh(\zeta) - 2}{4A_{\text{sat}}} + \frac{3A_{\text{sat}}\epsilon\Gamma e^{-\zeta}(5e^{2\zeta} + 6e^{\zeta} + 5)}{8} \right)\delta + O(\delta^2). \quad (24)$$

We note that Eq. (18) allows us to eliminate the zeroth-order terms of the expansion and the left hand-side of Eq. (24). Thus, we can further simplify the expression to

$$\left(\frac{2\cosh(\zeta) - 2}{4A_{\text{sat}}} + \frac{3A_{\text{sat}}\epsilon\Gamma e^{-\zeta}(5e^{2\zeta} + 6e^{\zeta} + 5)}{8} \right)\delta + O(\delta^2) = 0. \quad (25)$$

For this expression to hold to the leading order in δ, the coefficient of the first-order term must equal zero, yielding the convergence value,

$$\zeta^* = \ln\left(\frac{4\sqrt{-9A_{\text{sat}}^4(\epsilon\Gamma)^2 - 6A_{\text{sat}}^2(\epsilon\Gamma)} + 2 - 9A_{\text{sat}}^2(\epsilon\Gamma)}{15A_{\text{sat}}^2(\epsilon\Gamma) + 2} \right). \quad (26)$$

For the chosen parameter set, ζ^* is found to be 0.664, agreeing closely with the results in Fig. 4(a) (i.e., at approximately mass index 7 and beyond). Therefore, one may approximate a transitional wave's envelope via an exponential-decay envelope with a uniform index ζ^* and offset A_{sat} if the wave amplitude is close to the saturation value.

In Fig. 4(c), we present attenuation envelopes initiated at varying amplitudes starting at the first mass, and we compare the envelopes obtained via a spatially varying decay factor ζ found using Eq. (21) to those via a constant decay factor ζ^* from Eq. (26). We observe that, at initial amplitudes close to the saturation amplitude, the approximation using a ζ^* envelope is highly accurate.

IV. NUMERICAL VERIFICATION

To numerically verify the attenuation envelopes for the two types of nonlinear evanescent waves identified, we construct a sufficiently long monatomic chain and simulate the dynamics using scripts written in MATLAB. Solutions to the governing equation, Eq. (2), are computed via direct numerical integration using the MATLAB function ODE45. Two types of excitation are considered: initial-condition (IC) excitation and boundary-continuous (BC) excitation. The former excitation specifies the initial displacement and velocity for each mass based on values derived from the perturbation solution. The latter excites a quiescent system by prescribing continuous harmonic oscillation at the boundary mass identified by $j = 0$.

We first consider the IC excitation, with the initial conditions of each mass, $j \geqslant 1$, following Eq. (27),

$$u_j = A(j)\sin(j\mu_r),$$
$$\dot{u}_j = A(j)\bar{\omega}\cos(j\mu_r), \quad (27)$$

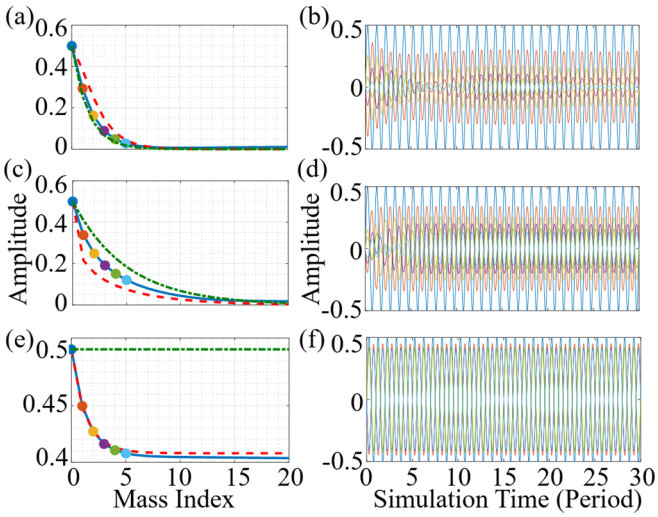

FIG. 5. Numerical verification of complete and transitional evanescent waves for initial-condition excitation. (a), (c), and (e) Comparison between perturbation-predicted (red dashed line), numerically simulated (blue solid line), and linear (green dash-dotted line) amplitude envelopes for hardening nonlinearity ($\bar{\omega} = 2.1$), softening nonlinearity ($\bar{\omega} = 2.01$), and softening nonlinearity ($\bar{\omega} = 1.95$) with saturation effect. The numerical time responses of the first five masses in the system are plotted on the right in panels (b), (d), and (f). The color of each curve in panels (b), (d), and (f) is associated with the color of the mass identified on the left.

where $A(j)$ denotes the amplitude of the jth mass according to the predicted attenuation envelope. The boundary mass $j = 0$ has a prescribed displacement $A\sin(\omega t)$ to remove the edge effect of the finite system. We confine our attention to the time evolution of the wave near the boundary $j = 0$. If the wave form specified by the initial conditions persists for ten periods, we confirm the perturbation-predicted result is a valid and stable solution to the problem.

Figure 5 depicts numerical results for the IC excitation for both complete evanescent waves [Figs. 5(a)–5(d)] and transitional evanescent waves [Figs. 5(e) and 5(f)]. The transitional evanescent wave solution here adopts the perturbation results in Eq. (21) with a spatially varying ζ. Note that the character of these solutions differ significantly from linear evanescent waves (i.e., the zeroth-order solutions), which have exponentially decaying envelopes. Overall, we observe good agreement between the qualitative shape and the quantitative predictions of the perturbation results and numerical simulations for hardening and softening complete evanescent waves in Figs. 5(a) and 5(c). The saturation effect shown in Fig. 5(e) also matches closely with the numerical results. Despite the transient behavior at the start of Fig. 5(b), the three time-history responses [Figs. 5(b), 5(d), and 5(f)] converge to their initial states, illustrating that the perturbation results on the left are sufficiently close to those generated by the governing equations.

We note that, compared to the linear amplitude envelope (green), the perturbation results (red) correctly predict the direction of the nonlinear shift. The small quantitative differences between perturbation results (blue) and numerical simulations (red) in Figs. 5(a) and 5(c) mainly arise from the

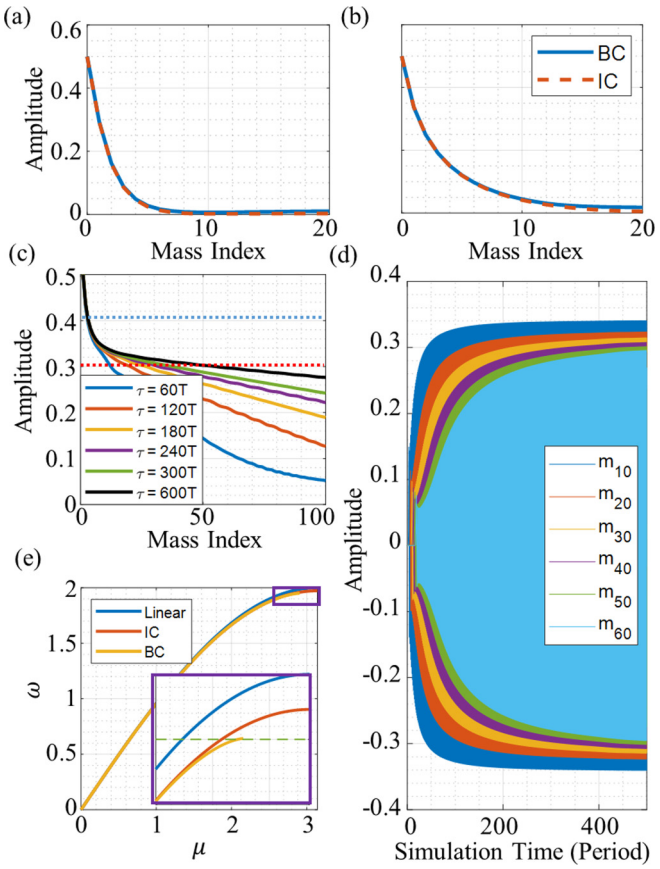

FIG. 6. Numerical verification with boundary-continuous excitation. (a) Numerical attenuation envelopes of a complete evanescent wave in a hardening system resulting from BC and IC excitation. (b) The numerical attenuation envelopes of a complete evanescent wave in a softening system resulting from BC and IC excitation. (c) The numerical attenuation envelope with selected simulation time (measured in excitation period T) for amplitude $A = 0.5$. The blue and red dashed lines indicate the saturation amplitude predicted from initial-condition excitation and boundary-continuous excitation, respectively. (d) Time responses of selected masses for $A = 0.5$. (e) Band-clipping effect on the studied system for $A = 0.3$. The green dashed line in the zoomed-in view denotes the excitation frequency.

amplitude assumption in Eq. (12), where the imaginary wave-number component is considered uniform across the triplet of masses—this assumption is relaxed in Fig. 5(e), where performance improves. As observed in the figures, this assumption provides very good approximations in the far field, but may generate small errors at the initial amplitude in the near field. Near-field improvements can likely be achieved by carrying out the perturbation analysis to higher orders.

For practical applications, the boundary-continuous excitation may be more appropriate as it appears in a large class of physical systems, such as thoe encountered when studying interface problems. In Fig. 6 we present numerical simulation results using a BC excitation. For complete evanescent waves, the BC excitation results in roughly the same attenuation envelope as the IC excitation, depicted in Figs. 6(a) and 6(b). Therefore, we confirm the perturbation solutions are capable of predicting complete evanescent waves excited from the boundary. For transitional evanescent waves, however, we observe a strong time dependency on the attenuation envelope and a lower saturation amplitude in Figs. 6(c) and 6(d).

In Fig. 6(c), the attenuation envelope rises in amplitude as the simulation time increases, and the rise is more pronounced in the far field than in the near field. This phenomena is due to the small group velocity at the excitation frequency close to the edge of the Brillouin zone. A small group velocity suggests a slow energy propagation and thus a longer time for energy to accumulate at each mass. In fact, the time to achieve the steady-state envelope increases for masses further away from the boundary excitation, as depicted in Fig. 6(d). Despite the strong time dependency, we observe a clear convergence tendency for the attenuation envelope in Fig. 6(c). The converging saturation amplitude is approximately $A = 0.3$, as highlighted by the red dashed line.

Of note in Fig. 6(c) is a discrepancy between the saturation amplitude observed in numerical simulations (red dashed line) versus that predicted by the perturbation analysis (blue dashed line). This discrepancy arises only in transitional evanescent waves under boundary-continuous excitation (and not under initial-condition excitation) and can be explained via the wave-number-space band-clipping phenomenon identified in Ref. [28] for nonlinear traveling waves excited at a boundary. Specifically, they noted that a boundary-excited harmonic wave in a weakly nonlinear system generates both a frequency shift and a wave-number clipping near the edge of the Brillouin zone, as reproduced in Fig. 6(e). This plot of traveling waves is generated using their iteration-based method at the observed saturation amplitude $A = 0.3$. In the zoomed-in view, we focus on the region near the cutoff frequency where the two nonlinear dispersion curves of traveling waves detach. We observe the dispersion curve from BC excitation (yellow) ends before reaching $\mu = \pi$ and exhibits a lower cutoff frequency than that of the IC excitation dispersion (red). As discussed in Sec. III C, at a saturation amplitude, the excitation frequency meets the cutoff frequency of the system. In Fig. 6(e), we observe the excitation frequency (green dashed line) lies close to the end of the BC excitation dispersion, which suggests the saturation amplitude for the system is approximately 0.3 with the wave-number band-clipping effect, agreeing with the numerical simulation results in Fig. 6(c). Since the system has softening nonlinearity, a larger amplitude is required to shift the IC excitation dispersion curve downwards to intersect the excitation frequency at $\mu = \pi$, which indicates a higher saturation amplitude for the IC excitation. Hence, we illustrate that the BC excitation results in a lower saturation amplitude and that this value can be calculated using the presented perturbation approach together with the band-clipping method proposed in Ref. [28].

V. CONCLUDING REMARKS

We investigated nonlinear evanescent waves in a cubic weakly nonlinear monatomic chain via a first-order Lindstedt-Poincaré perturbation approach. The perturbation results reveal that the wave-number's imaginary component is as a function of space. For frequencies higher than the linear cutoff frequency, the perturbation solutions predict a complete evanescent wave with a slower (hardening system) or

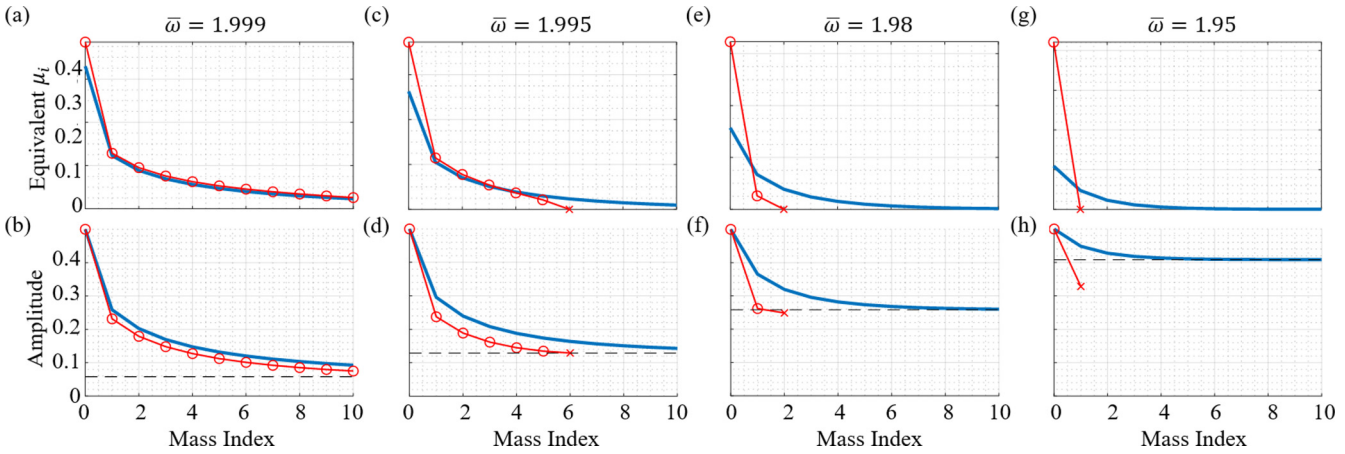

FIG. 7. The saturation effect derived from standard and modified perturbation results. Each column features the resultant imaginary wave-number component (top row) and attenuation envelope (bottom row) for selected frequencies. In each subfigure, blue solid curves denote the result from the modified perturbation result, and red solid curves denote the standard perturbation result. A round marker refers to a valid result, and a cross marker suggests an invalid once since the amplitude at this point is below the saturation amplitude indicated by the gray dashed line.

faster (softening system) decay rate than found in the linear system. For frequencies located in the NSE of a softening system, a transitional evanescent wave emerges with an amplitude saturation phenomenon—i.e., regardless of initial amplitude, the far-field amplitude converges to a finite value. The perturbation solution also suggests the envelope of such a system can be modeled as an exponential decay with a saturation amplitude offset. Direct numerical simulation of the governing equations verify the perturbation results and the saturation effect. We show that initial-condition excitation and boundary-continuous excitation lead to the same results for complete evanescent waves, but different saturation amplitudes for transitional evanescent waves. This phenomenon is qualitatively explained by a wave-number band-clipping phenomenon.

While the presented method generates quantitative results agreeing with numerical simulations, it also has restrictions inherent in the Lindstedt-Poincaré method. The method limits the analysis to a frequency shift and does not yield evolution equations for amplitude and phase, such as those found in averaging and multiple scales analysis. For the special case of BC-excited waves excited near the edge of the Brillouin zone, the presented analysis cannot directly capture clipping in the wave-number domain. Follow-on work is suggested which uses more advanced analysis tools to directly analyze these special cases. Lastly, we note that the developed perturbation analysis is broadly applicable and can be employed to study evanescent waves in a variety of discrete, nonlinear periodic structures.

ACKNOWLEDGMENTS

The authors would like to thank the National Science Foundation for support of this research under an Emerging Frontiers in Research and Innovation (EFRI) grant (Grant No. 1741565).

APPENDIX

We present in Fig. 7 the imaginary wave number and attenuation envelopes derived from the perturbation solution, Eq. (17), and the modified solution, Eq. (21). We observe that when the saturation amplitude is low, as shown in Figs. 7(a) and 7(b), the standard and modified solutions yield similar imaginary wave-number components and attenuation. However, as the saturation amplitude increases, the perturbation approach initially developed for complete evanescent waves predicts overestimated imaginary wave-number components that decrease the wave amplitude below the saturation amplitude. In addition, the higher the saturation amplitude, the less accurate this perturbation solution becomes. In the last column, Figs. 7(g) and 7(h), Eq. (17) predicts an overestimated imaginary wave-number component four times larger than that predicted by Eq. (21).

[1] L. Brillouin, *Wave Propagation in Periodic Structures: Electric Filters and Crystal Lattices* (Dover, New York, 1953), Vol. 2.

[2] C. Kittel, *Introduction to Solid State Physics*, 8th ed. (Wiley, New York, 2004).

[3] X.-L. Qi and S.-C. Zhang, Topological insulators and superconductors, Rev. Mod. Phys. **83**, 1057 (2011).

[4] C. He, X. Ni, H. Ge, X.-C. Sun, Y.-B. Chen, M.-H. Lu, X.-P. Liu, and Y.-F. Chen, Acoustic topological insulator and robust one-way sound transport, Nat. Phys. **12**, 1124 (2016).

[5] M. Gil, J. Bonache, and F. Martin, Metamaterial filters: A review, Metamaterials **2**, 186 (2008).

[6] J. Valentine, S. Zhang, T. Zentgraf, E. Ulin-Avila, D. A. Genov, G. Bartal, and X. Zhang, Three-dimensional optical metamaterial with a negative refractive index, Nature (London) **455**, 376 (2008).

[7] J. Li and C. T. Chan, Double-negative acoustic metamaterial, Phys. Rev. E **70**, 055602(R) (2004).

[8] M. D. Tocci, M. J. Bloemer, M. Scalora, J. P. Dowling, and C. M. Bowden, Thin-film nonlinear optical diode, Appl. Phys. Lett. **66**, 2324 (1995).

[9] H. Nassar, B. Yousefzadeh, R. Fleury, M. Ruzzene, A. Alù, C. Daraio, A. N. Norris, G. Huang, and M. R. Haberman, Nonreciprocity in acoustic and elastic materials, Nat. Rev. Mater. **5**, 667 (2020).

[10] J. Knight and D. Skryabin, Nonlinear waveguide optics and photonic crystal fibers, Opt. Express **15**, 15365 (2007).

[11] F. Li, P. Anzel, J. Yang, P. G. Kevrekidis, and C. Daraio, Granular acoustic switches and logic elements, Nat. Commun. **5**, 5311 (2014).

[12] M. D. Fronk and M. J. Leamy, Isolated frequencies at which nonlinear materials behave linearly, Phys. Rev. E **100**, 051002(R) (2019).

[13] P. B. Silva, M. J. Leamy, M. G. D. Geers, and V. G. Kouznetsova, Emergent subharmonic band gaps in nonlinear locally resonant metamaterials induced by autoparametric resonance, Phys. Rev. E **99**, 063003 (2019).

[14] Z. Wu and K.-W. Wang, On the wave propagation analysis and supratransmission prediction of a metastable modular metastructure for non-reciprocal energy transmission, J. Sound Vib. **458**, 389 (2019).

[15] R. K. Narisetti, M. Ruzzene, and M. J. Leamy, Study of wave propagation in strongly nonlinear periodic lattices using a harmonic balance approach, Wave Motion **49**, 394 (2012).

[16] X. Wang, W. Zhu, and M. Liu, Steady-state periodic solutions of the nonlinear wave propagation problem of a one-dimensional lattice using a new methodology with an incremental harmonic balance method that handles time delays, Nonlinear Dyn. **100**, 1457 (2020).

[17] M. H. Abedin-Nasab, M. V. Bastawrous, and M. I. Hussein, Explicit dispersion relation for strongly nonlinear flexural waves using the homotopy analysis method, Nonlinear Dyn. **99**, 737 (2020).

[18] X. Fang, J. Wen, J. Yin, and D. Yu, Wave propagation in nonlinear metamaterial multi-atomic chains based on homotopy method, AIP Adv. **6**, 121706 (2016).

[19] A. F. Vakakis and M. E. King, Nonlinear wave transmission in a monocoupled elastic periodic system, J. Acoust. Soc. Am. **98**, 1534 (1995).

[20] R. K. Narisetti, M. J. Leamy, and M. Ruzzene, A perturbation approach for predicting wave propagation in one-dimensional nonlinear periodic structures, J. Vib. Acoust. **132**, 031001 (2010).

[21] K. Manktelow, M. J. Leamy, and M. Ruzzene, Multiple scales analysis of wave–wave interactions in a cubically nonlinear monoatomic chain, Nonlinear Dyn. **63**, 193 (2011).

[22] K. Manktelow, M. J. Leamy, and M. Ruzzene, Comparison of asymptotic and transfer matrix approaches for evaluating intensity-dependent dispersion in nonlinear photonic and phononic crystals, Wave Motion **50**, 494 (2013).

[23] N. Z. Swinteck, K. Muralidharan, and P. A. Deymier, Phonon scattering in one-dimensional anharmonic crystals and superlattices: Analytical and numerical study, J. Vib. Acoust. **135**, 041016 (2013).

[24] M. D. Fronk and M. J. Leamy, Higher-order dispersion, stability, and waveform invariance in nonlinear monoatomic and diatomic systems, J. Vib. Acoust. **139**, 051003 (2017).

[25] M. D. Fronk and M. J. Leamy, Direction-dependent invariant waveforms and stability in two-dimensional, weakly nonlinear lattices, J. Sound Vib. **447**, 137 (2019).

[26] M. D. Fronk and M. J. Leamy, Internally resonant wave energy exchange in weakly nonlinear lattices and metamaterials, Phys. Rev. E **100**, 032213 (2019).

[27] S. R. Panigrahi, B. F. Feeny, and A. R. Diaz, Wave–wave interactions in a periodic chain with quadratic nonlinearity, Wave Motion **69**, 65 (2017).

[28] W. Jiao and S. Gonella, Wavenumber-space band clipping in nonlinear periodic structures, Proc. R. Soc. A **477**, 20210052 (2021).

[29] R. Khajehtourian and M. I. Hussein, Dispersion characteristics of a nonlinear elastic metamaterial, AIP Adv. **4**, 124308 (2014).

[30] G. Chakraborty and A. Mallik, Dynamics of a weakly nonlinear periodic chain, Int. J. Non-Linear Mech. **36**, 375 (2001).

[31] J. A. Kulpe, K. G. Sabra, and M. J. Leamy, Bloch-wave expansion technique for predicting wave reflection and transmission in two-dimensional phononic crystals, J. Acoust. Soc. Am. **135**, 1808 (2014).

[32] A. H. Nayfeh, D. T. Mook, and P. Holmes, *Nonlinear Oscillations* (Wiley, New York, 1980).

[33] I. Maksymov, L. Marsal, and J. Pallares, Finite-difference time-domain analysis of band structures in one-dimensional Kerr-nonlinear photonic crystals, Opt. Commun. **239**, 213 (2004).

[34] M. V. Komissarova, V. F. Marchenko, and P. Y. Shestakov, $\mathcal{PT}$-symmetric periodic structures with the modulation of the Kerr nonlinearity, Phys. Rev. E **99**, 042205 (2019).

[35] B. Deng, J. Raney, K. Bertoldi, and V. Tournat, Nonlinear waves in flexible mechanical metamaterials, J. Appl. Phys. **130**, 040901 (2021).

[36] S. P. Wallen and M. R. Haberman, Nonreciprocal wave phenomena in spring-mass chains with effective stiffness modulation induced by geometric nonlinearity, Phys. Rev. E **99**, 013001 (2019).

[37] M. I. Hussein, M. J. Leamy, and M. Ruzzene, Dynamics of phononic materials and structures: Historical origins, recent progress, and future outlook, Appl. Mech. Rev. **66**, 040802 (2014).